Characterization of helical states in semiconductor quantum wells using quantum information quantities

Natalia Giovenale, Omar Osenda

Facultad de Matemática, Astronomía, Física y Computación, Universidad Nacional de Córdoba e Instituto de Física Enrique Gaviola - CONICET, Av. Medina Allende s/n, Ciudad Universitaria, CP:X5000HUA Córdoba, Argentina,

Abstract

The information content of one-electron bulk and edge states in semiconductor quantum wells is calculated in the inverted regime, where edge states, topologically protected, are responsible for the conduction in Spin Quantum Hall effect experiments. To study the information content of these states we first calculate realistic two dimensional one-electron states, solving first the eight-band $\mathbf{k}\cdot\mathbf{p}$ Hamiltonian to obtain the bulk states and then a four band effective Hamiltonian to obtain the edge states. The behavior of information-like quantities, as a function of the different parameters that define the quantum well, is analyzed. The results presented show that the helical edge states can be singled out using different quantities that characterize the rich phenomenology of these states.

Keywords: Valid PACS appear here

1. Introduction

Semiconductors, and the nanostructures made of them, allow to investigate an incredible set of physical situations because, among other reasons, changing the density of charge carriers by several orders of magnitude is a routine task nowadays, and this leads to remarkably different scenarios. Since the experiments that led to the discovery of the Quantum Hall effect by Klaus von Klitzing [1], the semiconductor quantum well has become an ideal scenario to study a host of different phenomena: fractional Quantum Hall effect [2], Quantum Spin Hall effect [3, 4, 5] and condensation of excitons and polaritons [6, 7], just to name a few.

In the case of the Quantum Spin Hall effect, the properties of the helical edge states, which are topologically nontrivial [4], are fundamental to understand the conductance properties in HgTe quantum wells. The characterization of topological states can be done using at least two approaches: calculating a topological quantity, as the Chern number or the Z_2 number [3, 8, 9, 10], or calculating the entanglement entropy or entanglement spectrum of the state of interest [11, 12, 13]. The first approach mentioned can be implemented when the band structure is at disposal, while the second approach has been mostly used to study many-body models when the reduced density matrix of a subsystem, that is half the whole system, can be effectively calculated.

The entanglement entropy and the entanglement spectrum capture the non-local character of a topological state, and have been calculated for spin chain states [14, 15, 16, 17] and for states that are though to be good approximations of the many-electron ground state wave function of the fractional Quantum Hall effect, *i.e.* the Laughlin states [18, 12, 19, 20]. Other studies have analyzed the general properties of the entanglement spectrum of topological states in different physical setting and geometries [21, 22, 23, 24, 25, 26], and it is been used to reveal the presence of a Haldane phase [27, 28]. All in all, depending on the physical systems, sometimes the topological character is better put into evidence using the behaviour of an entanglement entropy, while in other situations the best tool is the entanglement spectrum.

Email addresses: ngiovenale@famaf.unc.edu.ar (Natalia Giovenale), osenda@famaf.unc.edu.ar (Omar Osenda)

Since the properties of electrons in semiconductor quantum wells are well described using the $\mathbf{k}\cdot\mathbf{p}$ model, it is quite natural to ask if the one-electron edge states obtained in this way can be analyzed using some of the techniques developed to study topological quantum states in quantum spin chains. There are two main difficulties to proceed along this idea. The first one has to do with the difficulties involved in obtaining realistic one-electron edge states. If a one-electron edge state is provided, then the second issue must be addressed: Which is the subsystem that is to be traced out to obtain the necessary reduced density matrix to calculate entanglement entropies and spectrum?

Realistic one-electron edge states in semiconductor quantum wells are quite difficult to calculate [29], in contradistinction with the spectrum, which can be obtained trough well educated guesses about the envelope functions that are the solutions of the eigenvalue problem for some multi-band Hamiltonian. The reasons behind this difference can be easily traced. Edge states depend on, at least, two coordinates, there are matching and contour conditions to be satisfied and the physical regimes of interest arise when there are a few bands that interact, making the calculation in terms of multi-band Hamiltonians mandatory. Recently, a number of works have addressed this issue and paved the way to obtaining robust edge states with and without an external magnetic field applied to the quantum well [30, 31, 32, 33]. The second difficulty mentioned above can be dealt with by using real-space entanglement [13], in which the subsystem that is traced out is a finite domain of one (or several) of the spatial coordinates of a given quantum state.

The aim of this paper is to study the properties of one-electron edge states confined in HgTe-CdTe quantum wells. This system has been extensively studied since it shows the appearance of helical edge states, which govern the transport properties in the Quantum Spin Hall (QSHE) and Quantum Hall (QHE) effects. Conductance experiments show, when the appropriate external magnetic field is applied, the presence of topological states. So, for quantum wells defined with parameters close to those of the QSHE regime, we obtain the edge states and characterize them using different quantum entropies, under the hypothesis that these entropies would put into evidence physical traits as localization, polarization and others.

The paper is organized as follows, the eight-band Kane Hamiltonian is presented in Section 2, together with the effective two-dimensional Hamiltonian. The details involved in the numerical calculations needed to obtain the bulk states and spectrum are deferred to Appendix A, while the corresponding details concerning the edge states are consigned in Appendix B. In both cases, bulk states and edge states, the Rayleigh-Ritz variational method is employed to obtain a high-precision numerical approximation for the spectrum and eigenstates. The study of the edge and normal states entropies is developed in Section 3, and some complementary results are included in Appendix C. In this Section we also present the definition of the spatial von Neumann entropy, the corresponding reduced density matrix and the numerical quantities that enter into the implementation of the Rayleigh-Ritz method. Finally, we present our conclusions and a discussion of our results in Section 4.

2. Kane Hamiltonian, effective Hamiltonian, bulk and edge states

Quantum Wells (QW) can be described as a sandwich of three semiconductor slabs, as pictured in Figure 1. In this cartoon, we represent the HgTe/$Cd_{0.7}Hg_{0.3}$Te QW that we study. As can be seen in this Figure, the middle slab, in blue, represents the HgTe slab, and has a width d known as the QW width. The outer slabs, in green, are made of $Cd_{0.7}Hg_{0.3}$Te, and considered of infinite width. There is a critical value of the QW width, d_c, for which the transport properties of the system change as a result of the band inversion [4]. In HgTe/$Cd_{0.7}Hg_{0.3}$Te QW's, this value is $d_c \sim 6.3$ nm. If $d < d_c$ the transport regime is normal and the bands are not inverted, while for $d > d_c$, the Quantum Hall regime, the transport occurs along the (x, y) plane. From now on, we refer to this system as a HgTe/CdTe QW.

The band structure of semiconductor quantum wells can be obtained studying the 8-band $\mathbf{k}\cdot\mathbf{p}$ Hamiltonian, but a full numerical treatment of a two dimensional problem with this Hamiltonian is quite taxing. So, to obtain the edge state wave functions, it is necessary to make use of an effective Hamiltonian [30], which is obtained from the bulk approximated states of the infinite quantum well. In the following subsection, the procedure to obtain the edge states is roughly described, but more specific details can be found in Appendix A and Appendix B.

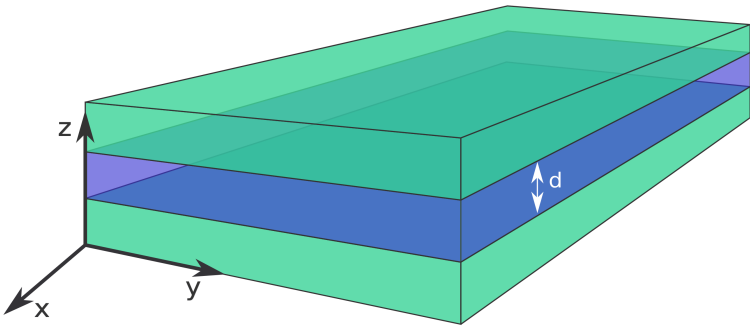

Figure 1: The cartoon depicts the layered structure that forms the quantum well. From bottom to top, there are three layers composed of $Cd_{0.7}Hg_{0.3}Te$, HgTe and $Cd_{0.7}Hg_{0.3}Te$, respectively. The middle layer has a width d in the z direction, that is transversal to the three slabs. The reference coordinate system is also depicted in the lower left corner of the cartoon.

2.1. Eight-band Kane Hamiltonian and bulk states

If the quantum well is infinite, or more precisely, if there is not any boundary conditions at finite values of the x or y coordinates, the electronic band structure of the quantum well can be calculated using the Kane Hamiltonian [34]

$$H = \begin{pmatrix}
T & 0 & -\frac{1}{\sqrt{2}}Pk_+ & \sqrt{\frac{2}{3}}Pk_z & \frac{1}{\sqrt{6}}Pk_- & 0 & -\frac{1}{\sqrt{3}}Pk_z & -\frac{1}{\sqrt{3}}Pk_- \\
0 & T & 0 & -\frac{1}{\sqrt{6}}Pk_+ & \sqrt{\frac{2}{3}}Pk_z & \frac{1}{\sqrt{2}}Pk_- & -\frac{1}{\sqrt{3}}Pk_+ & \frac{1}{\sqrt{3}}Pk_z \\
-\frac{1}{\sqrt{2}}k_-P & 0 & U+V & -\bar{S}_- & R & 0 & \sqrt{\frac{1}{2}}\bar{S}_- & -\sqrt{2}R \\
\sqrt{\frac{2}{3}}k_zP & -\frac{1}{\sqrt{6}}k_-P & -\bar{S}_-^\dagger & U-V & C & R & \sqrt{2}V & -\sqrt{\frac{3}{2}}\tilde{S}_- \\
\frac{1}{\sqrt{6}}k_+P & \sqrt{\frac{2}{3}}k_zP & R^\dagger & C^\dagger & U-V & \bar{S}_+^\dagger & -\sqrt{\frac{3}{2}}\tilde{S}_+ & -\sqrt{2}V \\
0 & \frac{1}{\sqrt{2}}k_+P & 0 & R^\dagger & \bar{S}_+ & U+V & \sqrt{2}R^\dagger & \frac{1}{\sqrt{2}}\bar{S}_+ \\
-\frac{1}{\sqrt{3}}k_zP & -\frac{1}{\sqrt{3}}k_-P & \frac{1}{\sqrt{2}}\bar{S}_-^\dagger & \sqrt{2}V & -\sqrt{\frac{3}{2}}\tilde{S}_+^\dagger & \sqrt{2}R & U-\Delta & C \\
-\frac{1}{\sqrt{3}}k_+P & \frac{1}{\sqrt{3}}k_zP & -\sqrt{2}R^\dagger & -\sqrt{\frac{3}{2}}\tilde{S}_-^\dagger & -\sqrt{2}V & \frac{1}{\sqrt{2}}\bar{S}_+^\dagger & C^\dagger & U-\Delta
\end{pmatrix}, \quad (1)$$

where

$$k_\pm = k_x \pm ik_y\,, \quad (2)$$

$$k_z = -i\partial_z. \quad (3)$$

The diagonal terms of the Hamiltonian have a "kinetic energy" shape, and introduce the lowest energy of the bulk conduction band, E_c, and the largest energy of the bulk valence band, $E_v(z)$. For instance,

$$T = E_c(z) + \frac{\hbar^2}{2m_0}\left[(2F+1)(k_x^2+k_y^2) + k_z(2F+1)k_z\right]. \quad (4)$$

The other entries on the Hamiltonian in Equation (1), and the meaning and values of the material parameters, as m_0, F and E_c in Equation 4, are given in Appendix A.

The bulk band structure of the system can be obtained by solving the eigenvalue problem

$$H\Psi = E_B\,\Psi, \quad (5)$$

where E_B are the energy eigenvalues which form the bulk band structure, and Ψ are eight-band spinors, whose components, Ψ_i, are the solutions to the eigenproblem with eight coupled equations of the form

$$\sum_{j=1}^{8}\mathbf{H}_{i,j}\Psi_j(z) = E_B\,\Psi_i(z), \quad (6)$$

for $i = 1, 2, .., 8$, where $\mathbf{H}_{i,j}$ is the matricial one-coordinate differential operator that is obtained from Equation 1, replacing k_x and k_y by the x and y components of a vector belonging to the first Brillouin zone of the semiconductor. The behavior of the electrons is effectively described by the resulting one-coordinate Hamiltonian, since the problem is translational invariant in the x and y directions.

To solve the eigenproblems in Equation 6 we employ the Rayleigh-Ritz variational method. This method, in combination with the 8-band Kane Hamiltonian, has been successfully used to obtain the band structure of different semiconductor nanostructures [35, 36, 30]. As a result, the bulk eigenstates for the quantum well are obtained, and can be written as

$$\psi(x, y, z) = e^{ik_x x + ik_y y} \sum_{j=1}^{8} \Psi_j(z)|j\rangle \tag{7}$$

where $|j\rangle$ is the basis of the Kane Hamiltonian. For details about the implementation of the Rayleigh-Ritz method and the basis set used to solve the ploblem see Appendix A.

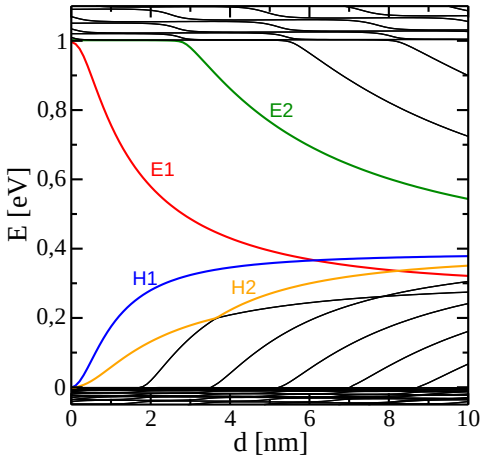

Figure 2: Spectrum of the HgTe/CdTe quantum well, as a function of the width of the HgTe layer, d. The sub-bands $E2$ (green line), $E1$ (red line), $H1$ (blue line) and $H2$ (orange line) are highlighted to better appreciate the eigenvalue crossing that separates both regimes. For $d < d_c$ the system is in the normal regime, $E_1 > H_1$, while for $d > d_c$ the band ordering is reverted.

Figure 2 shows the effect over the band structure of increasing the width d of the HgTe layer. The bottom and top of the conduction and valence bulk bands, respectively, of the system can be appreciated as the black bands of energies above 1.5 eV and below zero (we adopt the convention that the top of the valence band corresponds to 0 eV). It can be seen that there are energy levels that detach from both bands, and they are more numerous for increasing values of the width d. The convention used to name them is quite straightforward, those that come off from the conduction band are denoted as En, where n is a natural number that corresponds to the detachment order. The levels that become detached from the valence band are denoted by Hn. Figure 2 also shows the band inversion phenomena near $d_c \sim 6.3$ nm. As can be seen, the energy of the $E1$ sub-bands falls bellow that of the $H1$ sub-band around $d = d_c$. As d increases, more of this sub-band crossings occur.

2.2. Broken symmetry Effective Hamiltonian and edge states

When the quantum well is finite in one direction of the (x, y) plane, edge states appear under certain configurations. Following the most used convention, we consider a finite stripe in the y-direction, of length $2L = 1000$ nm. To model this situation, homogeneous boundary conditions have to be imposed in $y = -L/2$ and $y = L/2$ to the electron spinor components Ψ_j when solving the Hamiltonian in Equation 1. Moreover, in this configuration the quantum well has translational invariance only on the x direction, so now $k_y = -i\partial_y$,

and the basis set functions for solving the coupled equations in Equation 6 are functions of both y and z, which increases considerably the dimensions of the matrix representation of the eigenproblem.

A solution to this problem was proposed in Reference [30]. Keeping in mind that near the region of interest, *i.e.*, for energies close to the band gap energy, the transport behaviour is dominated by the $E1, E2, H1$ and $H2$ sub-bands [31, 30], and using perturbation theory [37, 31], the eigenstates that correspond to this sub-bands, that are obtained by the procedure described in Section 2.1, are used to generate an effective Hamiltonian of the form

$$\mathbf{H}_{eff} = \begin{pmatrix} \mathcal{H}(+k) & 0 \\ 0 & \mathcal{H}^*(-k) \end{pmatrix}, \tag{8}$$

where $\mathcal{H}$ is a 4×4 differential operator in the y coordinate, and $\mathcal{H}^*$ is its complex conjugate. The broken symmetry between the states and eigenvalues is clear, since the eigenvalues and eigenstates corresponding to positive values of k_x are calculated using $\mathcal{H}$, while the ones with negative values of k_x are obtained with $\mathcal{H}^*$.

Obtaining the eigenstates and eigenvalues of the Hamiltonians $\mathcal{H}$ and $\mathcal{H}^*$ can be done in a similar fashion as the one described in Section 2.1. Consider the associated eigenproblems

$$\mathcal{H}(+k)\Phi_+(y) = E_+\Phi_+(y), \tag{9}$$

and

$$\mathcal{H}^*(-k)\Phi_-(y) = E_-\Phi_-(y), \tag{10}$$

where $E_\pm$ are the eigenvalues of the band structure of the finite quantum well, $\Phi_\pm$ are four-band spinors and $\pm$ stands for the sign of k_x.

The components of $\Phi_\pm$ are obtained by solving the eigenproblem with four coupled equations for each value of k_x, in a similar way as in Equation 6. As a result, the spectum of the effective Hamiltonian as a function of k_x is obtained, and the edge eigenstates can be written as

$$\phi(x, y, z) = e^{ik_x x} \sum_{i=1}^{4} \Phi_{\pm,i}|i\rangle_\pm \tag{11}$$

where $|i\rangle_\pm$ are the bulk states, dependent on z, which form the basis of the effective Hamiltonian. For details about the operators $\mathcal{H}$, its basis, and more details of how to solve the eigenproblem, see Appendix B.

Figure 3 shows the spectrum of the effective Hamiltonian as a function of k_x for $d = 7$ nm (left panel) and $d = 9$ nm (rigth panel). The helical edge states can be easily identified, since they lay in the gap between sub-bands, and are represented by the light blue an pink lines. For $d = 7$ nm the helical states appear in the gap between the $H1$ and $E1$ sub-bands, and between H_1 and E_2 for $d = 9$ nm. Note that in both cases the system is in the inverted regime, see Figure 2. The spectra in Figure 2 are in very good agreement with the ones obtained from the Kane Hamiltonian for small values of k_x [30]. Figure 3 also shows that, in the absence of an external magnetic field, the spectra are symmetric as functions of k, *i.e.*, $E_+(+k) = E_-(-k)$. This is not the case when a magnetic field is applied, as will be shown in the next section. Note that the presence of edge states transforms the system, whose energy spectrum is given in Figure 2, in a gapless one. The closure of the gap forms a Dirac's cone, that is a well known signal of the presence of topological states.

2.3. Two-dimensional varational eigenstates

Collecting the results from the previous sections, and as a result of some calculations summarized in the Appendixes, we are now in condition to express the two-dimensional edge states of the system.

As stated before, the eigenfunctions of the Kane Hamiltonian, Equation 1, that correspond to the $E1$, $E2$, $H1$ and $H2$ sub-bands, for spin up and spin down, are the basis in which the effective Hamiltonian is written. So, each of the components of the eigenfunctions of $\mathcal{H}$ and $\mathcal{H}^*$, $\Phi_{\pm,i}$, is accompanied by the corresponding sub-band eigefunction. The two-dimensional variational eigenstates can then be expressed as

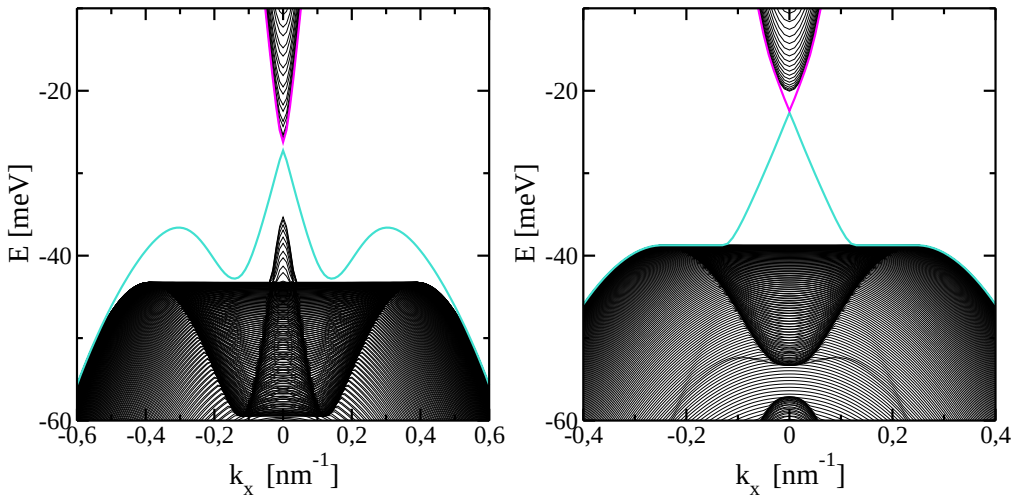

Figure 3: Spectrum of $\mathbf{H}_{eff}$ as a function of k_x, for $d = 7$ nm in the left panel, and $d = 9$ nm in the right panel. The bulk eigenvalues correspond to the black solid lines, while the energy of the edge states corresponds to the light blue and pink lines. The gap between sub-bands is closed by the edge states for $k = 0$.

$$|\phi(y,z)\rangle_{\pm} = \sum_{i,k,n,p} \alpha_{n,p}^{i,k,\pm} \psi_n(y) B_p(z) |k\rangle, \tag{12}$$

where $i = 1, .., 4$ and $\pm$ corresponds to the effective Hamiltonian eigenstates, $|k\rangle$ for $k = 1, .., 8$ is the Kane Hamiltonian basis, ψ_n for $n = 1, .., N$ are the functions in Equation B.7, and B_p for $p = 1, .., M$ are $B-$spline functions [38, 39]. The coefficient $\alpha_{n,p}^{i,k,\pm}$ contains the coefficients involved in Equations A.10, B.6 and B.8.

In what follows, we will focus in the characterization of the behaviour of the localized edge states, $|\phi(y,z)\rangle_{\pm}$, for given values of the parameters B and k_x, the strength of the magnetic field applied in the z direction and the wave vector in the only direction that does not have finite boundary conditions for the variational eigenstates, respectively. This election for the direction of the magnetic field is not the most general, but corresponds to the most common experimental settings. Also, this choice has several analytical advantages, since the magnetic field dependent effective Hamiltonian keeps the block structure of Equation 8.

3. Results: Characterization of states using information-like quantities

One of the best known quantum information quantifiers is the von Neumann entropy, which is given by

$$S(\rho_A) = -\mathrm{Tr}\rho_A \log_2(\rho_A). \tag{13}$$

where ρ_A, the reduced density operator of a state ρ_{AB} of a composite system with subsystems A and B, is given by

$$\rho_A = \mathrm{Tr}_B \rho_{AB}, \tag{14}$$

Diagonalizing the matrix representation of the operator ρ_A, the von Neumann entropy can be calculated as

$$S(\rho_A) = -\sum_{\ell} \lambda_\ell \log_2(\lambda_\ell), \tag{15}$$

where λ_ℓ are the eigenvalues of ρ_A.

There are many papers devoted to study the information content of topological-like states in spin chains [14, 15, 16, 17] and in systems with continuum degrees of freedom [18, 12, 19, 20]. Note that, in spin chains,

the natural way to express the total Hilbert space is as the tensorial product of subsystems which are given by complementary segments of the chain. The usual procedure to obtain reduced density matrices consists in tracing out a segment of the chain, and the information content is calculated through a given quantum entropy associated to this reduced density matrix.

The intricate way in which the variational eigenstates approximations to the helical edge states depend on many different variables, see Equation 12, could lead to a number of possible partitions of the Hilbert space, and each one would result in a different characterisation of the states. In the following, we will study a few of such possibilities, by means of the so called real space entropy [13] defined for two dimensional systems. Considering the subsystems A and B as

$$A = \text{the whole } z \text{ coordinate axis}, \qquad B = \mathcal{D}, \tag{16}$$

where $\mathcal{D}$ is a domain defined in the y coordinate, the real space entropy is the the von Neumann entropy of the reduced density matrix that result from this election. Tracing out a coordinate to obtain a reduced density matrix as a mean to study the properties of the quantum state of a single particle was introduced in Reference [40], and has been used to analyze the behavior of Laguerre-Gaussian one-photon states [41] and the binding of resonance states [42], among other applications (see Reference [13] and References therein).

For the eigenfunctions $|\phi\rangle_{\pm}$ (Equation 12) obtained using the variational method, we proceed to calculate a real space entropy by tracing out, from the two-coordinate one-particle state

$$\rho = |\phi\rangle_{\pm\,\pm} \langle\phi| \,, \tag{17}$$

a spatial domain $\mathcal{D}$ in the y coordinate. From now on, we omit the suffix $\pm$ of the effective Hamiltonian basis for clarity. In this way, we construct a one-coordinate reduced density matrix

$$\rho_{\mathcal{D}}(z, z') = \frac{1}{N} \int_{\mathcal{D}} |\phi(y, z)\rangle \langle\phi(y, z')| \, dy, \tag{18}$$

where

$$N = \int \int_{\mathcal{D}} |\phi(y, z)\rangle \langle\phi(y, z)| \, dy \, dz, \tag{19}$$

and $|\phi\rangle$ stands for $|\phi\rangle_+$ or $|\phi\rangle_-$. From now on, $\rho_{\mathcal{D}}$ stands for the reduced density matrix obtained by tracing out the subsystem $B = \mathcal{D}$.

The eigenvalues λ_ℓ of the reduced density operator in Equation 18, needed to calculate the real space entropy of the state, are obtained solving the integral equation

$$\int \rho_{\mathcal{D}}(z, z')\varphi_\ell(z') \, dz' = \lambda_\ell \varphi_\ell(z), \tag{20}$$

where $\varphi_\ell(z)$ are the eigenfuntions of the reduced density matrix. This problem can be cast into an algebraic eigensystem problem, by choosing a set of basis functions and diagonalizing the reduced density matrix. Note that once the subsystem B has been traced out, the remaining density operator depends on the $B-$spline functions and the Kane Hamiltonian basis, so this two sets of functions are the natural choice for a basis to write the reduced density matrix. The entries of the reduced density matrix are then given by

$$[\rho_{\mathcal{D}}]_{ka,lb} = \frac{1}{N} \sum_{i,n,p} \sum_{j,m,q} (\alpha^{i,k,\pm}_{n,p})^* \alpha^{j,l,\pm}_{m,q} I^{\mathcal{D}}_{nm} S_{a,p} S_{q,b}, \tag{21}$$

where k and l are the indixes for the Kane basis, a and b correspond to the $B-$spline basis,

$$N = \sum_{i,k} \sum_{n,m} \sum_{p,q} (\alpha^{i,k,\pm}_{n,p})^* \alpha^{j,l,\pm}_{m,q} S_{p,q} I^{\mathcal{D}}_{nm}, \tag{22}$$

$$I^{\mathcal{D}}_{nm} = \int_{\mathcal{D}} \psi^\star_n(y) \psi_m(y) \, dy \quad \text{and} \quad S_{p,q} = \langle B_p | B_q \rangle. \tag{23}$$

Note that when $\mathcal{D}$ is equal to the whole y axis then

$$I^{\mathcal{D}}_{nm} = \delta_{n,m}, \tag{24}$$

where δ is the Kronecker function.

The eigenfunctions $|\phi\rangle_{\pm}$ are either extended along the width of the quantum well, or strongly localized on its borders. This implies that there is not a natural choice for the domain $\mathcal{D}$, if the real space von Neumann entropy were to be used to distinguish between the different states that can be found between the eigenstates of Equation 8. In what follows we will focus on the results obtained when $\mathcal{D}$ is the whole y axis, while other chosings are deferred to Appendix C. Also, at the end of this section, we present the results obtained from an alternative entropy that we propose, which further characterize the states of the system.

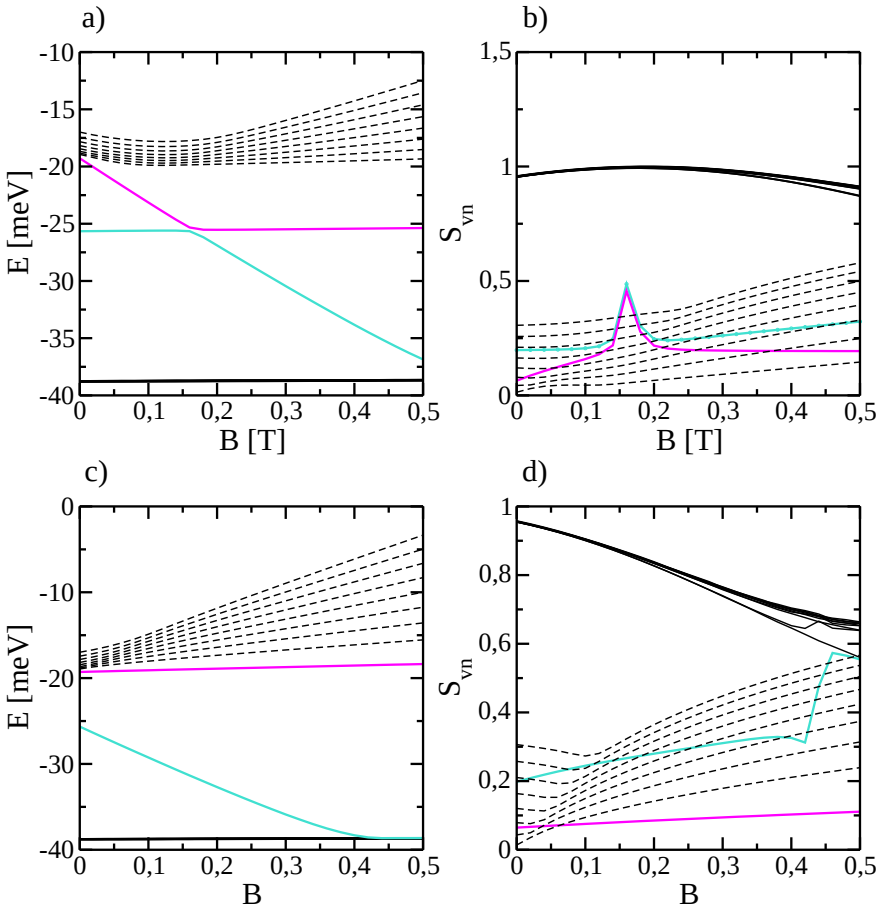

Figure 4: a) Energy spectrum of the effective Hamiltonian for a quantum well of width $d = 9$ nm as a function of the magnetic field intensity B, for $k_x = 0.02$ nm^{-1}. In full black lines are higher energy states of the valence band, the dashed black ones correspond to the lowest energy states of the conduction band, and the pink (highest energy in the gap) and light blue (lowest energy in the gap) lines correspond to the two edge states. b) real space entropy calculated for $\mathcal{D}$ as the whole y axis. The parameters are the same as in a), and the color code corresponds to the same states in both panels. Panels c) and d) have the same information as panels a) and b), respectively, but for $k_x = -0.02$ nm^{-1}

The results that we present correspond to a very reduced set of parameters (k, d and B), nevertheless they are representative of the physical traits that are observed for other values of those parameters. For choosing the quantum well parameters, some considerations must be taken into account. First, from Figure 3 it is clear that for very small values of k the helical states are farther away from the bottom and top of the conduction and valence bands, respectively. Also, the various perturbations made to obtain the Kane and

effective Hamiltonians, results in accurate solutions for small values of this parameter. Second, when an external magnetic field is applied the helical states eventually enter into the conduction or valence bands. The actual value of the magnetic fields for which the helical states enter the bands depend on k, the width d, etc. The value of k and the magnitude of the magnetic field are proportionally inverse, so some compromise in choosing the value of k has to be made.

3.1. Real space - von Neumann entropy for normal and edge states

In this subsection, we consider the real space entropy when $\mathcal{D}$ is the whole y coordinate.

Figure 4 a) shows the spectrum of the effective Hamiltonian, for a quantum well of width $d = 9$ nm, as a function of the magnetic field strength B, for $k_x = 0.02$ nm^{-1}. The figure shows only several variational eigenvalues of the conduction and valence bands, using dashed and continuous black lines, respectively. The helical edge states energies are shown by the light blue and pink lines, the same color code used in Figure 3. Panel b) shows the behaviour of the real space entropy for those states included in panel a). Panels c) and d) are equivalent to panels a) and b), respectively, but correspond to $k_x = -0.02$ nm^{-1}. The curves in panels b) and d) show an "inverted ordering" with respect of panel a) and c), meaning that the valence band states have larger entropies that the states in the conduction band.

The values of the real space entropy of the states considered, show that the helical states have the same symmetries as the states of the valence band, which are $H1$ states, *i.e.*, hole-like states. This behaviour was found for several values of k_x and d, since not matter the value of this parameters, the bottom a the valence band is always the $H1$ bulk sub-band. This is not the case for the top of the conduction band, which is the $E2$ sub-band for $d = 7,8$ nm and $H2$ for $d = 9$ nm [30].

3.2. Decomposing the Hilbert space in a different way

The results obtained concerning the real space entropy shown in Figure 4 suggest that other quantity to measure the localization on the y coordinate and the strong polarization of the helical edge states is needed.

As said before, the elections that can be made of two subsystems for obtaining an information-like entropy are several. Nonetheless, the mathematical features of the edge states obtained using the methods described, leaves a reduced number of options since it is not always possible to write the Hilbert space as a tensor product. An alternative for this treatment is to consider an entropy that is calculated for the hole states, without tracing out a part of the Hilbert space. Many of these quantities were considered in this work, in which we calculated the von Neumann entropy taking into consideration different partitions of the coefficients of the eigenstates obtained.

In this sense, the simpler quantity one can consider is given by

$$S^{edge} = \sum_n \sum_i |d_n^{i,\pm}|^2 \log(|d_n^{i,\pm}|^2) \tag{25}$$

where the sum in n is over the eigenbasis in the y direction of, and the one in i is over the basis of the effective Hamiltonian. The coefficients $d_n^{i,\pm}$ corresponds to the solutions of the effective Hamiltonian (see Appendix B).

Note that the S^{edge} entropy is fairly similar to the real space entropy, if the z coordinate were the one traced out.

Figure 5 a) and c) show the energy spectra of a quantum well of width $d = 9$ nm as a function of the magnetic field, for $k = 0.01$ nm^{-1} and $k = -0.01$ nm^{-1} respectively. The valence band is depicted by black lines, while the conduction band is in dashed black lines. The light blue and pink lines are the helical edge states in this configuration. Panels b) and d) in Figure 5 show the S^{edge} entropy for the states in panels a) and c) respectively. The strong polarization of the helical edge states is clearly put into evidence by this measure, since they present entropies grater than any of the bulk states close in energy. A clear differentiation of helical edge states, from normal states, is obtained from this quantity, which virtually does not change for these two states in the parameter interval shown.

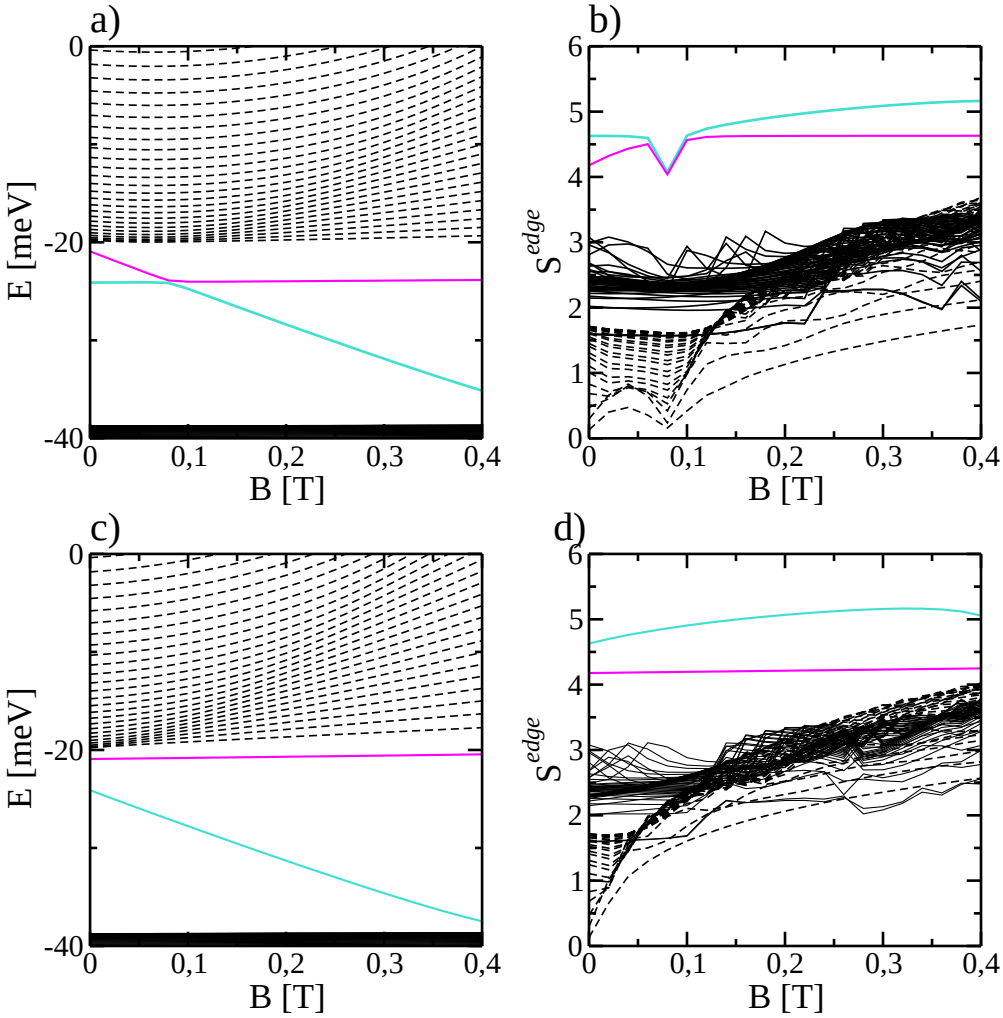

Figure 5: a) Energy spectrum of the effective Hamiltonian for a quantum well of width $d = 9$ nm as a function of the magnetic field intensity B, for $k_x = 0.01$ nm^{-1}. The valence band is depicted in black lines, la dashed black lines correspond to the conduction band, and the light blue and pink ones correspond to the edge states energies. b) S^{edge} entropy for the states corresponding to the energies included in a). The color code corresponds to the same states in both panels. Panels c) and d) have the same information as panels a) and b), respectively, but for $k_x = -0.01$ nm^{-1}

4. Discussion and Conclusions

Even in spite of the simplification that implies to treat the two dimensional problem using an effective Hamiltonian, which effectively reduces the dimensionality of the numerical algorithms needed to find the edge states, the whole procedure is quite taxing and CPU time consuming. Nevertheless, we have tested the characterization of edge states using different entropies for values of the width $d = 7$ nm, $d = 8$ nm and $d = 9$ nm, and for a variety of values of k and B for each value of d. In all the analyzed cases, the behavior observed was, qualitatively, the same that the one shown in Figures 4, 5 and C.6. It is clear that different choices for the subspace that is traced out result in a different characterization of the helical edge states. Most notably, S^{edge} clearly identifies the edge states as those that possess more information among the states that are close to the band gap. Even more, this information is almost independent on the strength of the external magnetic field. It would be interesting to study if this trait remains under magnetic impurities.

In both Figures 4 and 5 we do not include states that lie too far away from the conduction band bottom or the valence band top. There are at least two reasons to proceed in this way. The first has to do with the continuum nature of the energy in the bands which makes it difficult to envisage how a given state can be separated from another one that lies close to it in energy. The Rayleigh-Ritz method represents the continuous bands with a discrete set of eigenvalues, whose density is a good approximation to the ideal density of states, but the relationship between the continuum states and the variational ones becomes harder to grasp when states that lie far away from the gap are considered.

The second reason that supports that the states far from the gap should not be considered comes from the fact that the effective Hamiltonian is obtained using a *perturbative* expansion, using the sub-bands states $E1$, $E2$, $H1$ and $H2$. Into the conduction and valence bands, especially in the later, there is a strong mixing between the sub-bands associated to the sub-bands $E1$ and $H2$, leading to a variational spectrum full of crossings and avoided crossings which make very difficult to follow the state of a single eigenvalue, or even the eigenvalue. This phenomenon is well known and has been pointed in different studies concerning systems with external magnetic fields applied to them where the avoided crossings come from continua associated to different Landau Levels [42, 36, 43].

A closely related subject is the stability of the numerical energy and spinors helical edge states found using the Rayleigh-Ritz method. The values of the energy are rather easily obtained, at least for $k \neq 0$. For $k = 0$ it is known that there is no gap between the two helical edge states [30]. This feature is particularly difficult to be obtained using the variational method, requiring very large basis sets of ψ_n functions. Nevertheless, as can be appreciated in Figure 3, for large enough basis sets size (> 2000) the variational spectrum is gapless with an error lesser than 10^{-3} meV. The other features of the spectrum and entropies are very stable. It is clear that the large basis set sizes are necessary because the helical edge states are localized over lengths that are much more smaller than the length of the slab in the y direction, nevertheless the value considered is compatible with realistic setups.

As can be seen in Figure C.6, the study of the real-space entanglement, measured through the von Neumann entropy, is able to quantify and characterize the localized behavior of edge states. The behavior of the von Neumann entropy separates clearly the localized edge states from the extended bulk ones. Even tough the calculus of the different steps necessary to obtain the von Neumann entropy is full of intricacies, it is interesting that the difference between each kind of states can be so clearly appreciated.

The domains that we choose to calculate reduced density matrices are not the only possible choices. Choosing disjoint segments A and B is one of the more attractive possibilities that come to mind. We are working along these lines of research. Other issues worth of further investigation includes the effect of external magnetic fields with components in the (x, y) plane, higher dimensional effective Hamiltonians and the possibility to consider a full two-dimensional treatment of the Kane Hamiltonian.

Acknowledgements

We acknowledge SECYT-UNC and CONICET (PIP-11220150100327CO) for partial financial support. We also want to thank Hernán L. Calvo for fruitful discussions about the physics of edge states and Mariano Garagiola for the help with the implementation of the numerical algorithms in the first stages of the investigation leading to this article.

Appendix A. Bulk Espectrum and states

The matrix elements of the Kane Hamiltonian in Equation 1 are operators given by

$$T = E_c(z) + \frac{\hbar^2}{2m_0}\left[(2F+1)(k_x^2+k_y^2) + k_z(2F+1)k_z\right], \tag{A.1}$$

$$U = E_v(z) - \frac{\hbar^2}{2m_0}\left[\gamma_1(k_x^2+k_y^2) + k_z\gamma_1 k_z\right], \tag{A.2}$$

$$V = -\frac{\hbar^2}{2m_0}\left[\gamma_2(k_x^2+k_y^2) - 2k_z\gamma_2 k_z\right], \tag{A.3}$$

$$R = -\frac{\hbar^2}{2m_0}\frac{\sqrt{3}}{2}\left[(\gamma_3-\gamma_2)k_+^2 - (\gamma_3+\gamma_2)k_-^2\right], \tag{A.4}$$

$$\bar{S}_\pm = -\frac{\hbar^2}{2m_0}\sqrt{3}k_\pm\left[\{\gamma_3,k_z\} + \{\kappa,k_z\}\right], \tag{A.5}$$

$$\tilde{S}_\pm = -\frac{\hbar^2}{2m_0}\sqrt{3}k_\pm\left[\{\gamma_3,k_z\} - \frac{1}{3}\{\kappa,k_z\}\right], \tag{A.6}$$

$$C = \frac{\hbar^2}{m_0}k_-\left[\kappa,k_z\right]. \tag{A.7}$$

where

$$k_\pm = k_x \pm ik_y, \tag{A.8}$$

$$k_z = -i\partial_z. \tag{A.9}$$

In Equation A.8, k_x and k_y can be either differential operators or vectors in the Brillouin zone, if the quantum wells has boundary conditions in those coordinates or not, respectively. From Equation A.1 trough A.7, all the parameters involved are characteristic of the semiconductor, $E_c(z)$ and $E_v(z)$ are the conduction and valence band edges, γ_1, γ_2 and γ_3 are the Luttinger parameters, Δ is the spin-orbit energy, κ and F take into account the interaction with far-lying bands and P is the Kane momentum matrix element. The values for the material parameters used are listed in Table A.1. As usual, $[A,B]$ and $\{A,B\}$ are the commutator and anticommutator of operators A and B, respectively.

	$E_g(eV)$	$\Delta(eV)$	$E_p(eV)$	F	γ_1	γ_2	γ_3	κ
CdTe	1.606	0.91	18.8	-0.09	1.47	-0.28	0.03	-1.31
HgTe	-0.303	1.08	18.8	0	4.1	0.5	1.3	-0.4

Table A.1: Parameter in the Kane Hamiltonian por CdTe and HgTe[34]

The eigenvalues shown in Figure 2 where obtained using a high-precision variational method with B-spline functions [38, 39], $\{B_i\}$, as the variational basis set in the z direction. The B-spline basis set has a number of properties that make them well suited to analyze the one-dimensional eigenproblem in Equation 6. In particular, they can be tuned to fulfill the discontinuous derivative of the functions Ψ_i at the interface between different materials accommodating any boundary condition (see Reference [44] and References therein). For this reason, although its use is not that common in the context of solving Shcrödinger equations, when compared with the number in which they have been applied in few-body Quantum Mechanics (see References [39, 38] and references therein, there are several works that use them when multidimensional spinors are involved, as are the cases of $\mathbf{k}\cdot\mathbf{p}$ Hamiltonians [44, 35] and Dirac Hamiltonians [45, 46].

Basis sets used for solving eigenproblems are, naturally, finite. This transforms the exact eigenvalue problem into a variational one that can be solve applying the Rayleigh-Ritz method. In the $B-$spline basis, the eigenstates components for this problem can be expanded as

$$\Psi_i(z) = \sum_{p=1}^{M} c_p^i B_p(z), \tag{A.10}$$

where the index $i = 1, 2, .., 8$ indicates the component correspondent to the $i-$th element of the basis of the Kane Hamiltonian, and $p = 1, 2, .., M$ is the spline function index. For obtaining the coefficients c_p^i, and the variational spectrum associated to these states, the eigenvalue problems in Equation 6 needed to be solved are now

$$\sum_{j=1}^{8}\sum_{q=1}^{M}\bar{\mathbf{H}}_{ip,jq}c_q^j = E_B S_{pq}c_q^i \,, \tag{A.11}$$

for $i = 1, .., 8$ and $p = 1, .., M$, where $\bar{\mathbf{H}}_{ip,jq} = \langle B_p|\mathbf{H}_{ij}|B_q\rangle$, $S_{pq} = \langle B_p|B_q\rangle$ and M is the variational basis set size.

Another advantage in the use of $B-$spline functions in this problem comes from the fact that they are compact support functions. This allows, in a very simple way, to change the density of functions used in some areas of the spatial domain. In this way, in our calculations we took $M = 150$, assigning 50 grid point to the HgTe slab, and 50 to each of the CdTe slabs, even while the former one is considerably smaller. This was chosen in order to have a better representation of the state that would be localized into the well (HgTe slab) while minimizing numerical effort and also it reflects the discontinuity given by the material interfaces on the spinor components. For more details on $B-$spline functions and the properties mentioned above, see References [44, 38, 39] and References therein.

Appendix B. Edge spectrum and states

The explicit form of the $\mathcal{H}$ operators in the effective Hamiltonian in Equation 8 is given by

$$\mathcal{H}(\mathbf{k}) = \begin{pmatrix} \epsilon_{\mathbf{k}} + d_3(\mathbf{k}) & -Ak_+ & R_1k_-^2 & S_0k_- \\ -Ak_- & \epsilon_{\mathbf{k}} - d_3(\mathbf{k}) & 0 & R_2k_-^2 \\ R_1k_+^2 & 0 & \epsilon_{H2}(\mathbf{k}) & A_2k_+ \\ S_0k_+ & R_2k_+^2 & A_2k_- & \epsilon_{E2}(\mathbf{k}) \end{pmatrix} \tag{B.1}$$

where

$$\begin{aligned} \mathbf{k} &= (k_x, k_y)\,, & \text{(B.2)}\\ \epsilon_{\mathbf{k}} &= C - D(k_x^2 + k_y^2)\,, & \text{(B.3)}\\ \epsilon_{H2} &= C - M - \Delta_{H1H2} + B_{H2}(k_x^2 + k_y^2)\,, & \text{(B.4)}\\ \epsilon_{E2}(\mathbf{k}) &= C + M + \Delta_{E1E2} + B_{E2}(k_x^2 + k_y^2)\,, & \text{(B.5)} \end{aligned}$$

wehre Δ_{H1H2} (Δ_{E1E2}) is the gap energy between the $H1$ and $H2$ ($E1$ and $E2$) sub-bands when $\mathbf{k} = 0$, and all of the other parameter involved are given in Table B.2. When solving the eigenvalue problem for a finite stripe in the y coordinate, k_x becomes the x coordinate of a vector in the first Brillouin zone, and $k_y = -i\partial_y$.

The basis in which this Hamiltonian is expresed are the states $|E1,+\rangle\,|H1,+\rangle\,|H2,-\rangle\,|E2,-\rangle$, and the basis correspondent to $\mathcal{H}^*$ is $|E1,-\rangle\,|H1,-\rangle\,|H2,+\rangle\,|E2,+\rangle$. The eigenstates corresponding to this sub-bands can be obtained from the solutions of the Kane Hamiltonian as following

$$\begin{aligned} |En,+\rangle &= \Psi_1^{(En,+)}|1\rangle + \Psi_4^{(En,+)}|4\rangle + \Psi_7^{(En,+)}|7\rangle,\\ |En,-\rangle &= \Psi_2^{(En,-)}|2\rangle + \Psi_5^{(En,-)}|5\rangle + \Psi_8^{(En,-)}|8\rangle\\ |Hn,+\rangle &= \Psi_3^{(Hn,+)}|3\rangle\\ |Hn,-\rangle &= \Psi_6^{(Hn,-)}|6\rangle \end{aligned} \tag{B.6}$$

where $\{|k\rangle\}_{k=1}^{8}$ is the basis of the Kane Hamiltonian, and the functions $|En,+\rangle$ and $|Hn,+\rangle$ are functions with spin up while $|En,-\rangle$ and $|Hn,-\rangle$ are functions with spin down. The notation $\Psi_i^{(E,s)}$ indicates the $i-$th

d(nm)	$C^{\{1\}}$	$M^{\{1\}}$	$\Delta^{\{1\}}_{H1H2}$	$\Delta^{\{1\}}_{E1E2}$	$B^{\{2\}}$	$D^{\{2\}}$	
7	1.606	0.91	-0.28	0.03	18.8	-0.09	
9	-0.303	1.08	0.5	1.3	18.8	0	
d(nm)	$R^{\{2\}}_1$	$R^{\{2\}}_2$	$B^{\{2\}}_{H2}$	$B^{\{2\}}_{E2}$	$A^{\{3\}}_2$	$S^{\{3\}}_0$	$A^{\{3\}}$
7	-1006.74	-43.51	711.25	-29.99	336.13	44.70	1.47
9	-1154.64	-45.28	571.70	-38.94	312.21	57.30	4.1

Table B.2: Parameters for the effective Hamiltonian B.1 for a $HgTe - Cd_{0.7}Hg_{0.3}Te$ quantum well [30]. The units of the parameters are: meV for those indexed with $^{\{1\}}$t, meV·nm^2 for the ones with $^{\{2\}}$, and meV·nm for the ones with $^{\{3\}}$.

component of the eigenstates correspondent to the energy E and spin s of the sub-band under consideration (Hn or En).

The basis set used for solving the variational eigenvalue problem that derives from Equations 9 and 10 is given by

$$\psi_n(y) = \sqrt{\frac{2}{L}} \sin\left(\frac{n\pi}{L} y\right), \tag{B.7}$$

where L is the length of the strip, and $n = 1, 2.., N$. The value of N depends on the width of the quantum well. We found that the optimal value, comparing with the results from the Kane Hamiltonian, are $N = 1950$ for $d = 7$ nm, and $N = 2500$ for $d = 9$ nm. Note that the ψ_n functions satisfy the homogeneous boundary conditions at $y = -L/2$ and $y = L/2$. Each component of the variational eigenfunction of the effective Hamiltonian can then be expressed as

$$\Phi_{\pm,i} = \sum_{n=1}^{N} d_n^{i,\pm} \psi_n(y) \tag{B.8}$$

To analyze the behavior of the edge states when a magnetic field is applied to the quantum well along the z direction, both Hamiltonians, $\mathcal{H}(+k)$ and $\mathcal{H}^\star(-k)$ must be modified adding the Zeeman term, and using the Peierless substitution $\partial_i \longrightarrow \partial_i - \frac{e}{\hbar} A_i$. [47].

We compared our results with the corresponding results obtained previously by Krishtopenko *et al.* [30] and found that both sets of values differ in less than 0.005% across the region $k \in [-0.5, 0.5]$ nm^{-1}. We also calculated the spectra of bulk and edge states for quantum well widths of $d = 8$ nm and $d = 9$ nm, and found that the agreement with the results of Reference [30] was excellent in all the cases. These results are not included for the sake of brevity.

Appendix C. Real space entropy

To explore the spatial behaviour of the eigenstates $|\phi\rangle_\pm$ into account, we calculate von Neumann entropies for three qualitatively different domains, which are

$$\begin{aligned} \mathcal{D}_1 &: y \in \left[\frac{L}{2} - \Delta, \frac{L}{2}\right], \\ \mathcal{D}_2 &: y \in \left[\frac{L}{2}, \frac{L}{2} + \Delta\right], \\ \mathcal{D}_1 \cup \mathcal{D}_2 &: y \in \left[\frac{L}{2} - \Delta, \frac{L}{2} + \Delta\right], \end{aligned} \tag{C.1}$$

where $\Delta \in \left[0, \frac{L}{2}\right]$. So, using Equation 18, we obtain the reduced density matrices $\rho_{\mathcal{D}_1}$, $\rho_{\mathcal{D}_2}$ and $\rho_{\mathcal{D}_1 \cup \mathcal{D}_2}$, and then we compute their eigenvalues and the corresponding von Neumann entropies $S(\rho_{\mathcal{D}_1})$, $S(\rho_{\mathcal{D}_2})$ and

$S(\rho_{\mathcal{D}_1\cup\mathcal{D}_2})$ as functions of Δ. Besides, we calculate the quantity $S(\rho_{\mathcal{D}_1}) + S(\rho_{\mathcal{D}_2}) - S(\rho_{\mathcal{D}_1\cup\mathcal{D}_2})$, which is called the mutual information [48].

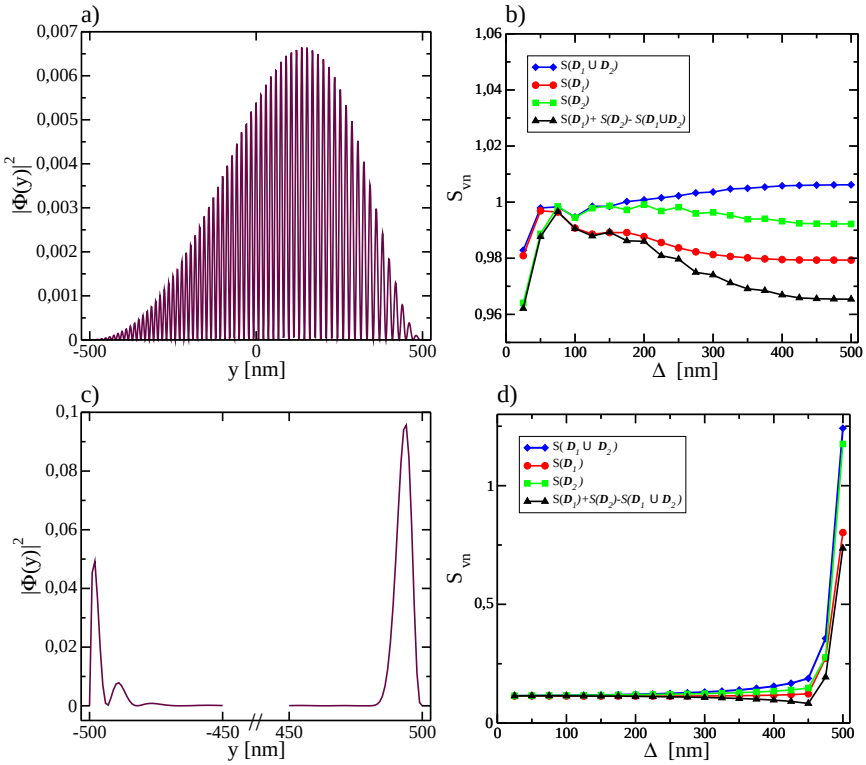

Figure C.6: The Figure shows a) the density probability $|\Phi(y)|^2$ for the state immediately bellow the edge state, as a function of y, while panel b) show the real space von Neumann entropy of the reduced density matrices $\rho_{\mathcal{D}}$, as a function of Δ, for the domains $\mathcal{D}_1 \cup \mathcal{D}_2$ (blue dots), $\mathcal{D}_1$ (red dots) and $\mathcal{D}_2$ (greendots), and the quantity $S(\rho_{\mathcal{D}_1}) + S(\rho_{\mathcal{D}_2}) - S(\rho_{\mathcal{D}_1\cup\mathcal{D}_2})$ (black dots). Panels c) and d) show the same quantities as a), b) for the edge state. The parameters of the system for this Figure are $d = 7$ nm, $B = 0.3$ T and $k_x = -0.29$ nm^{-1}.

As has been pointed out above, and is shown in Figure 3, the energy of the degenerate edge state lies in the gap between two sub-bands. This eigenvalue is degenerate if no magnetic field, B, is applied to the quantum well and the degeneracy is broken for $B \neq 0$. In what follows we will concentrate on the states on the gap and those immediately above and bellow belonging to the continuum, *i.e.* the top and bottom of the sub-bands that are separated by the gap.

The panel a) of Figure C.6 shows the behavior of $|\Phi(y)|^2$ versus the coordinate y. Panel b) shows the von Neumann entropies $S(\rho_{\mathcal{D}_1})$, $S(\rho_{\mathcal{D}_2})$ and $S(\rho_{\mathcal{D}_1\cup\mathcal{D}_2})$ and the quantity $S(\rho_{\mathcal{D}_1}) + S(\rho_{\mathcal{D}_2}) - S(\rho_{\mathcal{D}_1\cup\mathcal{D}_2})$ for the state lying at the top of the sub-band below the gap, all as functions of Δ. The data shown in Figure C.6 were obtained for $k_x = -0.29$ nm^{-1}, a magnetic field strength $B = 0.3$ T, and for a quantum well with $d = 7$ nm and $L = 1000$ nm. The extended nature of the state in panel a) is clearly manifested by $|\Phi(y)|^2$. The corresponding von Neumann entropies (panel b)) show a small change when Δ goes from zero to $L/2$, note the scale of the vertical axis. Interestingly the largest changes in the entropies are shown for relatively small values of Δ, around 100 nm. This behavior is attributable to the effect of the homogeneous boundary conditions over the envelope functions. Panels c) and d) of Figure C.6 show the same quantities that panels a) and b), for the same parameters of the system, but for the only edge state present in this configuration. The strong localization of the state near the quantum well edges, panel c), results in a very steep behavior of the entropies as can be seen in panel d).

It is worth to mention that the quantity $S(\rho_A) + S(\rho_B) - S(\rho_{A\cup B})$ has been proposed to analyze long range correlations, and topological phases and states [49]. We think that this quantity does not distinguish

in a clear way between bulk and edge states.

References

[1] K. v. Klitzing, G. Dorda, and M. Pepper. New method for high-accuracy determination of the fine-structure constant based on quantized hall resistance. *Phys. Rev. Lett.*, 45:494–497, Aug 1980. doi: 10.1103/PhysRevLett.45.494. URL https://link.aps.org/doi/10.1103/PhysRevLett.45.494.

[2] R. B. Laughlin. Anomalous quantum hall effect: An incompressible quantum fluid with fractionally charged excitations. *Phys. Rev. Lett.*, 50:1395–1398, May 1983. doi: 10.1103/PhysRevLett.50.1395. URL https://link.aps.org/doi/10.1103/PhysRevLett.50.1395.

[3] C. L. Kane and E. J. Mele. Quantum spin hall effect in graphene. *Phys. Rev. Lett.*, 95:226801, Nov 2005. doi: 10.1103/PhysRevLett.95.226801. URL https://link.aps.org/doi/10.1103/PhysRevLett.95.226801.

[4] B. Andrei Bernevig, Taylor L. Hughes, and Shou-Cheng Zhang. Quantum spin hall effect and topological phase transition in hgte quantum wells. *Science*, 314(5806):1757–1761, 2006. doi: 10.1126/science.1133734. URL https://www.science.org/doi/abs/10.1126/science.1133734.

[5] Markus König, Steffen Wiedmann, Christoph Brüne, Andreas Roth, Hartmut Buhmann, Laurens W. Molenkamp, Xiao-Liang Qi, and Shou-Cheng Zhang. Quantum spin hall insulator state in hgte quantum wells. *Science*, 318(5851):766–770, 2007. doi: 10.1126/science.1148047. URL https://www.science.org/doi/abs/10.1126/science.1148047.

[6] David Snoke. Spontaneous bose coherence of excitons and polaritons. *Science*, 298(5597):1368–1372, 2002. doi: 10.1126/science.1078082. URL https://www.science.org/doi/abs/10.1126/science.1078082.

[7] Wang Z, Rhodes DA, Watanabe K, Taniguchi T, Hone JC, Shan J, and Mak KF. Evidence of high-temperature exciton condensation in two-dimensional atomic double layers. *Nature*, 574(7776):76–80, 2019. doi: 10.1038/s41586-019-1591-7. URL https://www.nature.com/articles/s41586-019-1591-7#citeas.

[8] Rui Yu, Xiao Liang Qi, Andrei Bernevig, Zhong Fang, and Xi Dai. Equivalent expression of F_2 topological invariant for band insulators using the non-abelian berry connection. *Phys. Rev. B*, 84:075119, Aug 2011. doi: 10.1103/PhysRevB.84.075119. URL https://link.aps.org/doi/10.1103/PhysRevB.84.075119.

[9] Andreas P. Schnyder, Shinsei Ryu, Akira Furusaki, and Andreas W. W. Ludwig. Classification of topological insulators and superconductors in three spatial dimensions. *Phys. Rev. B*, 78:195125, Nov 2008. doi: 10.1103/PhysRevB.78.195125. URL https://link.aps.org/doi/10.1103/PhysRevB.78.195125.

[10] James de Lisle, Suvabrata De, Emilio Alba, Alex Bullivant, Juan J Garcia-Ripoll, Ville Lahtinen, and Jiannis K Pachos. Detection of chern numbers and entanglement in topological two-species systems through subsystem winding numbers. *New Journal of Physics*, 16(8):083022, aug 2014. doi: 10.1088/1367-2630/16/8/083022. URL https://doi.org/10.1088/1367-2630/16/8/083022.

[11] Alexei Kitaev and John Preskill. Topological entanglement entropy. *Phys. Rev. Lett.*, 96:110404, Mar 2006. doi: 10.1103/PhysRevLett.96.110404. URL https://link.aps.org/doi/10.1103/PhysRevLett.96.110404.

[12] Hui Li and F. D. M. Haldane. Entanglement spectrum as a generalization of entanglement entropy: Identification of topological order in non-abelian fractional quantum hall effect states. *Phys. Rev. Lett.*, 101:010504, Jul 2008. doi: 10.1103/PhysRevLett.101.010504. URL https://link.aps.org/doi/10.1103/PhysRevLett.101.010504.

[13] A. Sterdyniak, A. Chandran, N. Regnault, B. A. Bernevig, and Parsa Bonderson. Real-space entanglement spectrum of quantum hall states. *Phys. Rev. B*, 85:125308, Mar 2012. doi: 10.1103/PhysRevB.85.125308. URL https://link.aps.org/doi/10.1103/PhysRevB.85.125308.

[14] Sergei V. Isakov, Matthew B. Hastings, and Roger G. Melko. Topological entanglement entropy of a bose–hubbard spin liquid. *Nature Physics*, 7(10):772–775, Oct 2011. ISSN 1745-2481. doi: 10.1038/nphys2036. URL https://doi.org/10.1038/nphys2036.

[15] Hong-Chen Jiang, Zhenghan Wang, and Leon Balents. Identifying topological order by entanglement entropy. *Nature Physics*, 8(12):902–905, Dec 2012. ISSN 1745-2481. doi: 10.1038/nphys2465. URL https://doi.org/10.1038/nphys2465.

[16] Tarun Grover, Yi Zhang, and Ashvin Vishwanath. Entanglement entropy as a portal to the physics of quantum spin liquids. *New J. Phys.*, 15(2):025002, feb 2013. doi: 10.1088/1367-2630/15/2/025002. URL https://doi.org/10.1088/1367-2630/15/2/025002.

[17] Yirun Arthur Lee and Guifre Vidal. Entanglement negativity and topological order. *Phys. Rev. A*, 88:042318, Oct 2013. doi: 10.1103/PhysRevA.88.042318. URL https://link.aps.org/doi/10.1103/PhysRevA.88.042318.

[18] Masudul Haque, Oleksandr Zozulya, and Kareljan Schoutens. Entanglement entropy in fermionic laughlin states. *Phys. Rev. Lett.*, 98:060401, Feb 2007. doi: 10.1103/PhysRevLett.98.060401. URL https://link.aps.org/doi/10.1103/PhysRevLett.98.060401.

[19] O. S. Zozulya, M. Haque, K. Schoutens, and E. H. Rezayi. Bipartite entanglement entropy in fractional quantum hall states. *Phys. Rev. B*, 76:125310, Sep 2007. doi: 10.1103/PhysRevB.76.125310. URL https://link.aps.org/doi/10.1103/PhysRevB.76.125310.

[20] O. S. Zozulya, Masudul Haque, and Nicolas Regnault. Entanglement signatures of quantum hall phase transitions. *Phys. Rev. B*, 79:045409, Jan 2009. doi: 10.1103/PhysRevB.79.045409. URL https://link.aps.org/doi/10.1103/PhysRevB.79.045409.

[21] Andreas M. Läuchli, Emil J. Bergholtz, Juha Suorsa, and Masudul Haque. Disentangling entanglement spectra of fractional quantum hall states on torus geometries. *Phys. Rev. Lett.*, 104:156404, Apr 2010. doi: 10.1103/PhysRevLett.104.156404. URL https://link.aps.org/doi/10.1103/PhysRevLett.104.156404.

[22] Lukasz Fidkowski. Entanglement spectrum of topological insulators and superconductors. *Phys. Rev. Lett.*, 104:130502, Apr 2010. doi: 10.1103/PhysRevLett.104.130502. URL https://link.aps.org/doi/10.1103/PhysRevLett.104.130502.

[23] Didier Poilblanc. Entanglement spectra of quantum heisenberg ladders. *Phys. Rev. Lett.*, 105:077202, Aug 2010. doi: 10.1103/PhysRevLett.105.077202. URL https://link.aps.org/doi/10.1103/PhysRevLett.105.077202.

[24] Timothy H. Hsieh and Liang Fu. Bulk entanglement spectrum reveals quantum criticality within a topological state. *Phys. Rev. Lett.*, 113:106801, Sep 2014. doi: 10.1103/PhysRevLett.113.106801. URL https://link.aps.org/doi/10.1103/PhysRevLett.113.106801.

[25] Michael P. Zaletel, Roger S. K. Mong, and Frank Pollmann. Topological characterization of fractional quantum hall ground states from microscopic hamiltonians. *Phys. Rev. Lett.*, 110:236801, Jun 2013. doi: 10.1103/PhysRevLett.110.236801. URL https://link.aps.org/doi/10.1103/PhysRevLett.110.236801.

[26] L. Cincio and G. Vidal. Characterizing topological order by studying the ground states on an infinite cylinder. *Phys. Rev. Lett.*, 110:067208, Feb 2013. doi: 10.1103/PhysRevLett.110.067208. URL https://link.aps.org/doi/10.1103/PhysRevLett.110.067208.

[27] Frank Pollmann, Ari M. Turner, Erez Berg, and Masaki Oshikawa. Entanglement spectrum of a topological phase in one dimension. *Phys. Rev. B*, 81:064439, Feb 2010. doi: 10.1103/PhysRevB.81.064439. URL https://link.aps.org/doi/10.1103/PhysRevB.81.064439.

[28] Franco T. Lisandrini, Alejandro M. Lobos, Ariel O. Dobry, and Claudio J. Gazza. Topological kondo insulators in one dimension: Continuous haldane-type ground-state evolution from the strongly interacting to the noninteracting limit. *Phys. Rev. B*, 96:075124, Aug 2017. doi: 10.1103/PhysRevB.96.075124. URL https://link.aps.org/doi/10.1103/PhysRevB.96.075124.

[29] Benedikt Scharf, Alex Matos-Abiague, and Jaroslav Fabian. Magnetic properties of hgte quantum wells. *Phys. Rev. B*, 86: 075418, Aug 2012. doi: 10.1103/PhysRevB.86.075418. URL https://link.aps.org/doi/10.1103/PhysRevB.86.075418.

[30] S. S. Krishtopenko and F. Teppe. Realistic picture of helical edge states in hgte quantum wells. *Phys. Rev. B*, 97:165408, Apr 2018. doi: 10.1103/PhysRevB.97.165408. URL https://link.aps.org/doi/10.1103/PhysRevB.97.165408.

[31] S. S. Krishtopenko, W. Knap, and F. Teppe. Phase transitions in two tunnel-coupled hgte quantum wells: Bilayer graphene analogy and beyond. *Scientific Reports*, 6(1):30755, Aug 2016. ISSN 2045-2322. doi: 10.1038/srep30755. URL https://doi.org/10.1038/srep30755.

[32] Rafal Skolasinski, Dmitry I. Pikulin, Jason Alicea, and Michael Wimmer. Robust helical edge transport in quantum spin hall quantum wells. *Phys. Rev. B*, 98:201404, Nov 2018. doi: 10.1103/PhysRevB.98.201404. URL https://link.aps.org/doi/10.1103/PhysRevB.98.201404.

[33] Zewei Chen and Tai Kai Ng. Interaction-induced edge states in hgte/cdte quantum wells under a magnetic field. *Phys. Rev. B*, 99:235157, Jun 2019. doi: 10.1103/PhysRevB.99.235157. URL https://link.aps.org/doi/10.1103/PhysRevB.99.235157.

[34] E. G. Novik, A. Pfeuffer-Jeschke, T. Jungwirth, V. Latussek, C. R. Becker, G. Landwehr, H. Buhmann, and L. W. Molenkamp. Band structure of semimagnetic $Hg_{1-y}Mn_yTe$ quantum wells. *Phys. Rev. B*, 72:035321, Jul 2005. doi: 10.1103/PhysRevB.72.035321. URL https://link.aps.org/doi/10.1103/PhysRevB.72.035321.

[35] Natalia Giovenale and Omar Osenda. Study of the transition from resonance to bound states in quantum dots embedded on a nanowire using the $k \cdot p$ method. *Physica B: Condensed Matter*, 627:413564, 2022. ISSN 0921-4526. doi: https://doi.org/10.1016/j.physb.2021.413564. URL https://www.sciencedirect.com/science/article/pii/S0921452621007171.

[36] V V Ravi Kishore, B Partoens, and F M Peeters. Electronic and optical properties of core–shell nanowires in a magnetic field. *Journal of Physics: Condensed Matter*, 26(9):095501, feb 2014. doi: 10.1088/0953-8984/26/9/095501. URL https://doi.org/10.1088/0953-8984/26/9/095501.

[37] D G Rothe, R W Reinthaler, C-X Liu, L W Molenkamp, S-C Zhang, and E M Hankiewicz. Fingerprint of different spin–orbit terms for spin transport in HgTe quantum wells. *New J. Phys.*, 12(6):065012, jun 2010. doi: 10.1088/1367-2630/12/6/065012. URL https://doi.org/10.1088/1367-2630/12/6/065012.

[38] H Bachau, E Cormier, P Decleva, J E Hansen, and F Martín. Applications of B-splines in atomic and molecular physics. *Rep.Progr. Phys.*, 64(12):1815–1943, nov 2001. doi: 10.1088/0034-4885/64/12/205. URL https://doi.org/10.1088/0034-4885/64/12/205.

[39] C. de Boor. *A Practical Guide To Splines*. Springer, New York, 1978.

[40] M Ali Can, Alexander Klyachko, and Alexander Shumovsky. Single-particle entanglement. *J. Opt. B: Quantum Semiclass. Opt.*, 7(2):L1–L3, jan 2005. doi: 10.1088/1464-4266/7/2/l01. URL https://doi.org/10.1088/1464-4266/7/2/l01.

[41] Natalia Giovenale, Federico M. Pont, Pablo Serra, and Omar Osenda. Convexity properties of superpositions of degenerate bipartite eigenstates. *Phys. Rev. A*, 99:052340, May 2019. doi: 10.1103/PhysRevA.99.052340. URL https://link.aps.org/doi/10.1103/PhysRevA.99.052340.

[42] Mariano Garagiola, Federico M Pont, and Omar Osenda. Binding of two-electron metastable states in semiconductor quantum dots under a magnetic field. *Journal of Physics B: Atomic, Molecular and Optical Physics*, 51(7):075504, mar 2018. doi: 10.1088/1361-6455/aab1a0. URL https://doi.org/10.1088/1361-6455/aab1a0.

[43] Alba Y Ramos and Omar Osenda. Resonance states in a cylindrical quantum dot with an external magnetic field. *Journal of Physics B: Atomic, Molecular and Optical Physics*, 47(1):015502, dec 2013. doi: 10.1088/0953-4075/47/1/015502. URL https://doi.org/10.1088/0953-4075/47/1/015502.

[44] Mariano Garagiola and Omar Osenda. Excitonic states in spherical layered quantum dots. *Phys. E*, 116:113755, 2020. doi: https://doi.org/10.1016/j.physe.2019.113755. URL https://www.sciencedirect.com/science/article/pii/S1386947719305235.

[45] I P Grant. B-spline methods for radial dirac equations. *Journal of Physics B: Atomic, Molecular and Optical Physics*, 42(5):055002, feb 2009. doi: 10.1088/0953-4075/42/5/055002. URL https://doi.org/10.1088/0953-4075/42/5/055002.

[46] F. Fillion-Gourdeau, E. Lorin, and A.D. Bandrauk. Galerkin method for unsplit 3-d dirac equation using atomically/kinetically balanced b-spline basis. *Journal of Computational Physics*, 307:122–145, 2016. ISSN 0021-9991. doi: https://doi.org/10.1016/j.jcp.2015.11.024. URL https://www.sciencedirect.com/science/article/pii/S0021999115007640.

[47] M. V. Durnev and S. A. Tarasenko. Magnetic field effects on edge and bulk states in topological insulators based on HgTe/CdHgTe quantum wells with strong natural interface inversion asymmetry. *Phys. Rev. B*, 93:075434, Feb 2016. doi: 10.1103/PhysRevB.93.075434. URL https://link.aps.org/doi/10.1103/PhysRevB.93.075434.

[48] Michael M. Wolf, Frank Verstraete, Matthew B. Hastings, and J. Ignacio Cirac. Area laws in quantum systems: Mutual information and correlations. *Phys. Rev. Lett.*, 100:070502, Feb 2008. doi: 10.1103/PhysRevLett.100.070502. URL https://link.aps.org/doi/10.1103/PhysRevLett.100.070502.

[49] Yuhan Liu, Ramanjit Sohal, Jonah Kudler-Flam, and Shinsei Ryu. Multipartitioning topological phases by vertex states and quantum entanglement. *Phys. Rev. B*, 105:115107, Mar 2022. doi: 10.1103/PhysRevB.105.115107. URL https://link.aps.org/doi/10.1103/PhysRevB.105.115107.